NANO LETTERS

pubs.acs.org/NanoLett Letter

Observation of Ultrafast Self-Action Effects in Quasi-BIC Resonant Metasurfaces

Ivan S. Sinev,[‡] Kirill Koshelev,[‡] Zhuojun Liu,[‡] Anton Rudenko, Konstantin Ladutenko, Alexey Shcherbakov, Zarina Sadrieva, Mikhail Baranov, Tatiana Itina, Jin Liu, Andrey A. Bogdanov,* and Yuri Kivshar*

Cite This: *Nano Lett.* 2021, 21, 8848−8855 Read Online

ACCESS | Metrics & More | Article Recommendations

ABSTRACT: High-index dielectric metasurfaces can support sharp optical resonances enabled by the physics of bound states in the continuum (BICs) often manifested in experiments as quasi-BIC resonances. They provide a way to enhance light−matter interaction at the subwavelength scale bringing novel opportunities for nonlinear nanophotonics. Strong narrow-band field enhancement in quasi-BIC metasurfaces leads to an extreme sensitivity to a change of the refractive index that may limit nonlinear functionalities for the pump intensities beyond the perturbative regime. Here we study ultrafast self-action effects observed in quasi-BIC silicon metasurfaces and demonstrate how they alter the power dependence of the third-harmonic generation efficiency. We study experimentally a transition from the subcubic to supercubic regimes for the generated third-harmonic power driven by a blue-shift of the quasi-BIC in the multiphoton absorption regime. Our results suggest a way to implement ultrafast nonlinear dynamics in high-index resonant dielectric metasurfaces for nonlinear meta-optics beyond the perturbative regime.

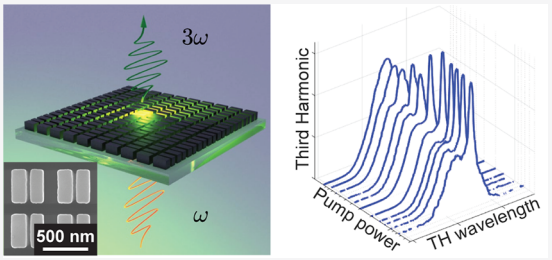

KEYWORDS: *Third-harmonic generation, metasurfaces, self-action effects, ultrafast optics, bound states in the continuum, nonperturbative regime*

Functional all-dielectric metasurfaces[1] rely on the fundamental concepts of structured arrays of subwavelength dielectric particles,[2−8] and they were suggested as a promising platform for enhancing the near-field intensities within the meta-atom volume required for various applications.[9] Due to low absorption losses, all-dielectric photonic structures became widely utilized for the enhancement of nonlinear and active phenomena, complementing more traditional plasmonic structures.[10,11] Very recently it was shown that dielectric metasurfaces with symmetry-broken meta-atoms can be employed to engineer sharp resonant response in reflection and transmission at the normal incidence associated with the physics of optical bound states in the continuum (BICs) .[12] In particular, it was shown that the in-plane asymmetry breaks destructive interference between leaky modes forming a quasi-BIC state that leads to controllable radiative losses being proportional to a square of the asymmetry parameter.

Quasi-BICs in asymmetric subwavelength metasurfaces are associated with Fano resonances,[13] trapped modes,[14] and metamaterial-induced transparency,[15] and they are employed in a number of applications targeting high-quality (high-Q) resonances in the infrared,[16] THz,[17] and microwave[18] frequency ranges, including biosensing,[19,20] enhanced light−matter interaction in two-dimensional materials,[21,22] manipulation of the far-field radiation patterns,[23] self-isolated Raman lasing,[24] and photosensitive tunability.[25] The crucial parameter for those applications is the maximum field enhancement at the resonance, which is reached at the critical coupling regime when the rates of the radiative losses and other losses coincide.[26] It was shown that the losses in the BIC metasurfaces are affected strongly by the presence of substrates and sample footprint, as well as disorder and surface roughness.[27] The asymmetry parameter for broken-symmetry metasurfaces with quasi-BIC resonances provides a tool for fine-tuning of the radiative losses, thus enabling further optimization of the field enhancement.[21]

For nonlinear metasurfaces, sharp resonances represent a natural way to enhance the parametric signal at the subwavelength scale beyond the traditional phase-matching.[28] Asymmetric dielectric metasurfaces supporting quasi-BIC

Received: August 22, 2021
Revised: October 6, 2021
Published: October 11, 2021

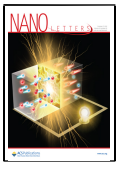

https://doi.org/10.1021/acs.nanolett.1c03257
Nano Lett. 2021, 21, 8848−8855

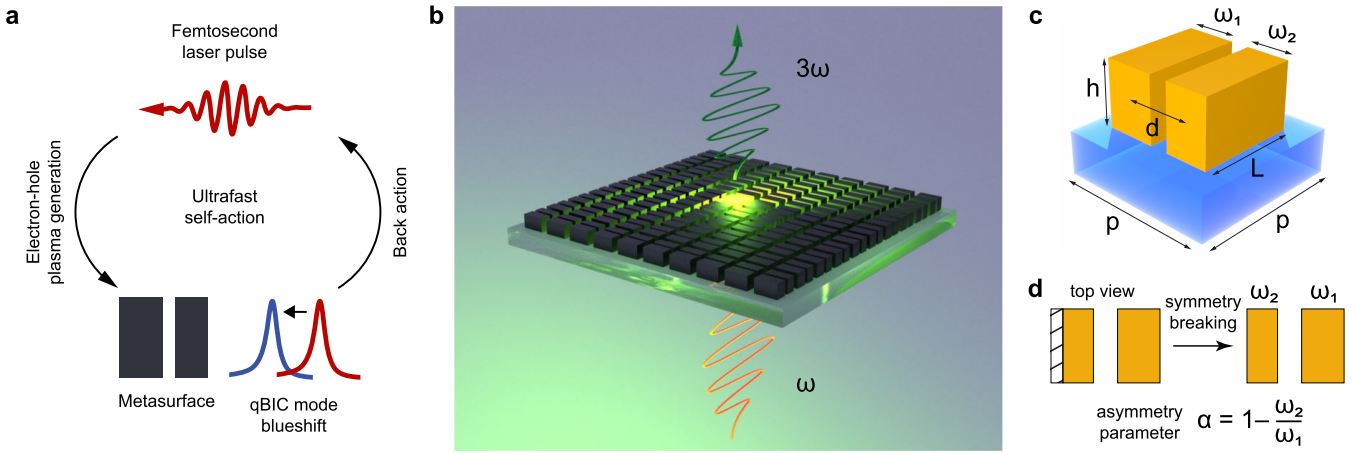

Figure 1. Silicon metasurface for THG and self-action effects. (a) Scheme of the ultrafast self-action effects in the qBIC metasurface. (b) Artistic view of third-harmonic generation from the metasurface with an asymmetric unit cell constructed from two parallel silicon nanobars. (c) Schematic view of the metasurface unit cell. The geometrical parameters used in the experiment and simulations are period p = 720 nm, bar length L = 550 nm, bar height h = 500 nm, lateral distance between bar centers d = 300 nm, bar width w_1 = 230 nm, and w_2 changes from 230 to 170 nm. (d) Definition of the asymmetry parameter α.

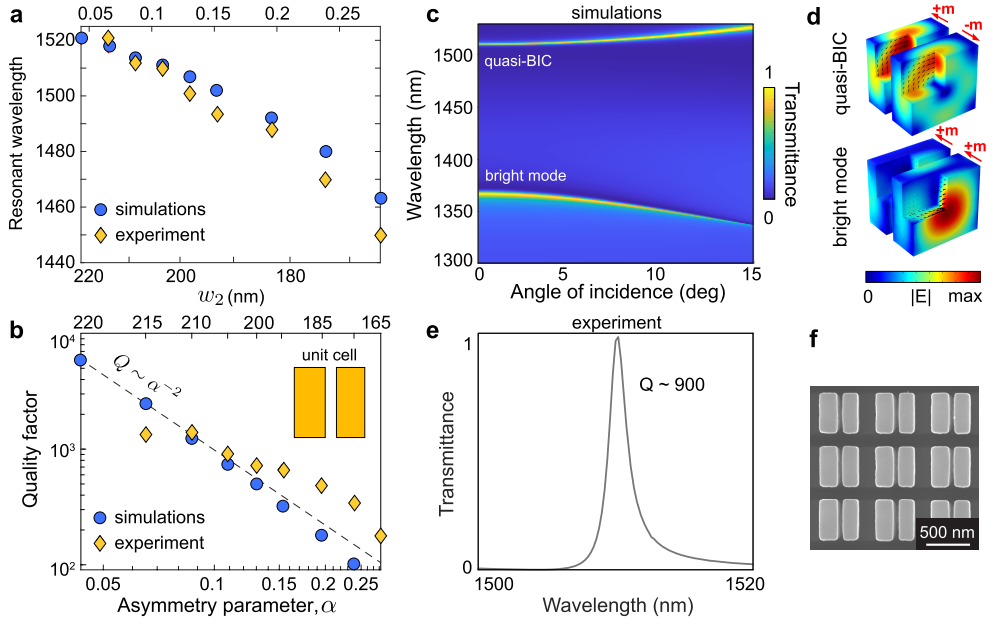

Figure 2. Measured and calculated resonant properties of quasi-BIC metasurfaces. (a) Calculated (blue) and measured (orange) resonant wavelength of quasi-BIC for different α. (b) Calculated (blue) and measured (orange) Q factors of quasi-BIC for different α. The dashed line shows the fit to the inverse quadratic law. The experiment shows saturation of the quality factor for small asymmetries which is due to the effect of parasitic losses. (c) Simulated angle-resolved transmittance spectrum of the metasurface with w_2 = 205 nm for TE polarization (with electric field of the incident wave directed along the bars). The quasi-BIC appears at 1510 nm wavelength and the bright mode is at 1370 nm. (d) Calculated electric field enhancement in the volume of silicon bars for the quasi-BIC and the bright mode. (e) Linear transmittance for the sample with w_2 = 205 nm. (f) SEM image of the metasurface with 9 unit cells. The scale bar (white) is 500 nm.

resonances were recently applied to improve the nonlinear conversion efficiency of second-harmonic,[29] third-harmonic,[30−32] and high-harmonic[33] generation processes. For high-intensity femtosecond pulses, material parameters of solids with strong nonlinear response, such as silicon, are substantially modified,[34] and the generation of harmonics with photon energies below the band gap is dominated by the generation of free carriers.[35] Subpicosecond transient second-order nonlinear response upon the ultrafast transfer of hot electrons has been demonstrated recently for an array of gold triangles placed on a slab of titanium dioxide.[36]

A rapid change of the material parameters due to strong field ionization effects leads to the self-action of laser pulses pumping a photonic structure.[37] In particular, ionization and consequent refractive index changes[38,39] lead to a spectral shift of the resonant wavelength with respect to the central frequency of the pulse. Recently, a blue-shift of the third-harmonic (TH) wavelength (also known as the photon acceleration effect) was observed in silicon metasurfaces supporting Mie resonances in the infrared range.[40] This provides a direct way to control the dynamics of linear and nonlinear signals on the time scales comparable with or even less than the pulse length,[41] as demonstrated in the recent

https://doi.org/10.1021/acs.nanolett.1c03257
Nano Lett. 2021, 21, 8848−8855

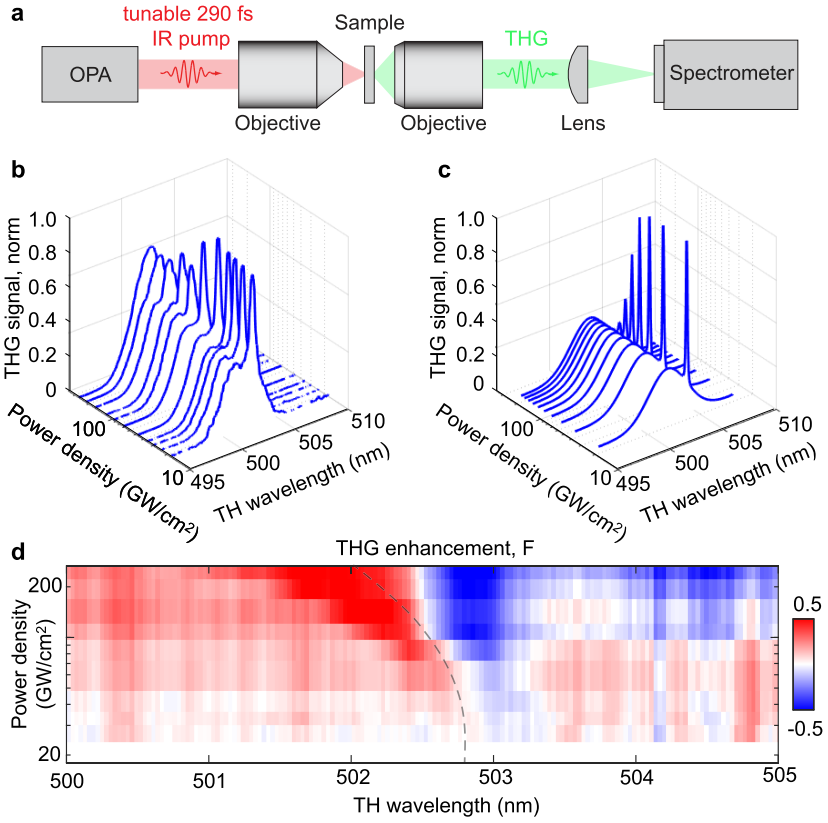

Figure 3. Self-action effects observed in THG. (a) Measurement setup of the THG spectra in transmission. (b) Dependence of THG spectra on pump power. Each spectrum is normalized to the third power of its pump intensity. (c) Calculated THG spectra for different pump powers. Normalization is the same as in panel b. (d) Power dependence of THG spectra illustrating the sub- (negative F) and supercubic (positive F) regimes for different detunings from the resonant wavelength. All spectra are normalized to the third power of the pump intensity as well as to the reference THG spectrum measured at the lowest pump power density (18 GW/cm^2) according to eq 1. The dashed line tracks the evolution of the spectral position of the THG peak.

experiments[42,43] with time-varying asymmetric metasurfaces. Self-action effects in metasurfaces with sharp resonances attract special attention because the strong field ionization regime can be realized even for moderate pump powers which in turn leads to an increase the mode line width of a high-Q resonance due to the generation of the electron−hole plasma in the material.[33]

Here, we study experimentally and theoretically the nonlinear ultrafast dynamics observed for the third-harmonic generation (THG) from resonant dielectric quasi-BIC metasurfaces. We engineer a silicon metasurface with an asymmetric unit cell composed of two parallel bars of different widths supporting a spectrally sharp transmission resonance in the near-IR with the Q factor of about 900. We demonstrate a drastic change of the THG power dependence from subcubic to supercubic regimes for average pump powers of a few mW. We observe a blue-shift of the TH wavelength above the threshold value of the pump power, and we associate this observation with the self-action effects of subpicosecond laser pulses (Figure 1a). We uncover that the self-action effects are driven by a strong field ionization in nanostructured silicon induced by the multiphoton absorption.

RESULTS AND DISCUSSION

Our metasurface consists of an array of silicon bar pairs placed on top of a glass substrate and arranged in a set of asymmetric square unit cells with period p = 720 nm (Figure 1b). The height of the bars is h = 500 nm and long side is L = 550 nm (Figure 1c). When the bars in the pairs are identical, the metasurface supports the symmetry-protected BIC at normal incidence for the polarization of light directed along the bars.[12] Introduction of the asymmetry parameter of the unit cell α controlled by a change of the width of one of the bars (Figure 1d) transforms BIC into quasi-BIC supporting high-Q leaky resonant modes[12] manifested in the transmission spectra as sharp Fano resonances.[44] We design the metasurface to support this high-Q mode in the telecom spectral range (1400−1600 nm) by making the bars in the unit cell w_1 = 230 nm wide (Figure 1d). The width of the smaller bar w_2 varies from 220 to 170 nm which corresponds to a change of the asymmetry parameter $\alpha = (1 - w_2/w_1)$ from 0 to 0.26. The lateral distance between the centers of the bars is fixed at d = 300 nm.

We calculate the eigenmode spectrum of the metasurface to analyze the resonant wavelength and Q factor of the quasi-BIC for different asymmetries. For numerical calculations, we use COMSOL Multiphysics software. The results are shown with blue circles in Figures 2a, b. The wavelength of quasi-BIC blue-shifts with an increase of asymmetry, while the Q factor drops to the value of about 100 for α = 0.25. The dependence of the Q factor on the asymmetry parameter follows the inverse square law $Q \sim \alpha^{-2}$ shown with a dashed line in Figure 2b. The simulated angle-resolved transmittance of the metasurface with w_2 = 205 nm ($\alpha \approx 0.11$) is shown in Figure 2c. The spectrum shows two pronounced resonances. The first one is the quasi-BIC resonance at 1510 nm; its line width narrows for smaller

https://doi.org/10.1021/acs.nanolett.1c03257
Nano Lett. 2021, 21, 8848−8855

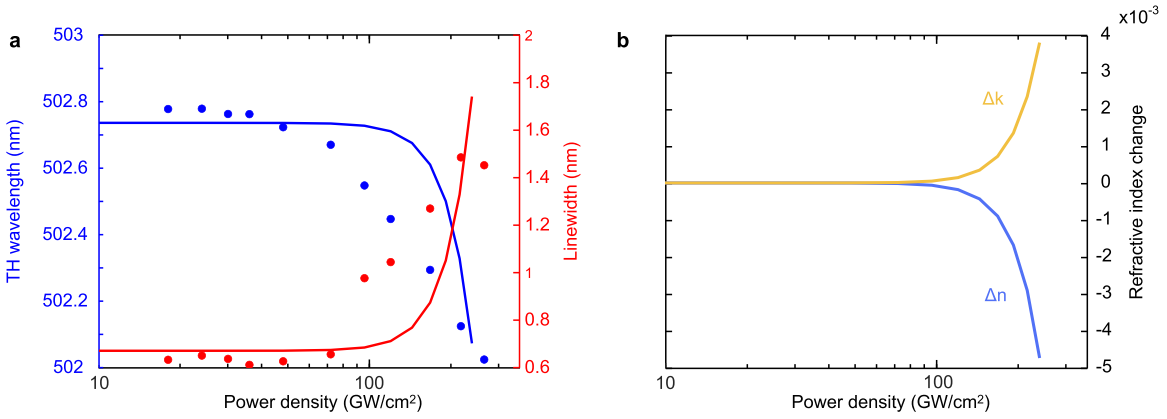

Figure 4. Properties of the third-harmonic radiation. (a) Measured (dots) and simulated (solid lines) evolution of the spectral position (blue) of the THG peak and its line width (red) with an increase of the pump power density. (b) Simulated evolution of the attenuation of real (blue) and imaginary (orange) parts of the refractive index of silicon in the metasurface with a growth of the pump power.

angles of incidence. The other resonance is driven by a bright mode at 1370 nm with a broad line width at the normal incidence since its quality factor $Q \approx 280$ is less than that of the quasi-BIC resonance. The electric field profiles of these two modes are shown in Figure 2d. The quasi-BIC resonance originates from interference of two magnetic dipoles (one in each bar) with close amplitudes and opposite phases, while for the bright mode the excited dipoles are in phase.

We fabricate a set of eight samples (see Materials and Methods below) with w_2 changing in the range 165, 185, 195, 200, 205, 210, 215, and 220 nm. We measure the linear transmittance spectrum for each sample and extract the resonant wavelength and Q factor of the quasi-BIC modes shown with the orange diamonds in Figures 2a, b. Minor differences in the calculated and measured resonant wavelengths can be explained by inhomogeneity of the sample and fabrication imperfections. The measured Q factor shown in Figure 2b saturates at a value of about 1500 due to the effect of dissipative losses, originating from a finite size of the sample, surface roughness, and structural disorder. The field enhancement and, consequently, the nonlinear currents inside the metasurface depend on the interplay of the radiative and dissipative losses, and it is maximized for the optimal coupling condition for which the total Q factor is two times smaller than its saturation value.[21,30] For further studies, we select the sample with $w_2 = 205$ nm because it is close to the optimal coupling condition. Figure 2 parts e and f show, respectively, the measured linear transmittance and scanning electron microscopy (SEM) image of the fabricated metasurface. The experimentally measured Q factor reaches a value of about 900.

Further, we study the metasurface-induced laser pulse self-action effects in the THG experiments. We intentionally use short (290 fs) laser pulses, even though such a duration is not optimal for the efficiency of the harmonic generation,[44] to facilitate the visualization of the spectral evolution of the mode in the TH spectra. We use optical parametric amplifier to tune the pump wavelength to the spectral range of the quasi-BIC and measure the TH signal in the transmission geometry, as illustrated in Figure 3a and described below in more detail (see Materials and Methods).

The evolution of the measured THG spectra with the pump power is shown in Figure 3b. The nonlinear spectra reveal a broad peak coming from the probe pulse and an additional sharp feature induced by the quasi-BIC resonance of the metasurface. As the pump power increases, the peak associated with the resonant mode demonstrates a gradual spectral blue-shift and broadening. The simulated evolution of the TH signal that accounts for the laser pulse self-action effects (see below) is shown in Figure 3c, and it is in a good qualitative agreement with the experimental data (the Fourier modal method was used[45]). Modifications of the mode parameters with an increase of the pump power lead to a spectrally dependent transition from sub- to supercubic regimes for the harmonic generation. We illustrate this effect by a map of the THG enhancement factor F with respect to the TH wavelength and pump power shown in Figure 3d. We define this quantity as follows:

$$F = \ln\left(\frac{I_{3\omega}(P)}{I_{3\omega}(P_0)\cdot(P/P_0)^3}\right) \quad (1)$$

where $I_{3\omega}(P)$ stands for the TH signal measured at the pump power P, and P_0 is the minimal pump power used in the experiment (18 GW/cm^2). In this way, the conventional third-power dependence of the TH signal would be represented as $F = 0$, and sub- and supercubic power dependencies are manifested as negative and positive values of F, respectively. The resulting map shown in Figure 3d reveals that, due to the power-dependent blue-shift of the quasi-BIC resonance, the TH signal demonstrates subcubic behavior that transforms to supercubic at lower wavelengths.

We attribute the transition effects from the sub- to supercubic regimes, resonance blue-shift, and its broadening to the laser-driven ultrafast generation of free carriers due to the multiphoton absorption that changes the material refractive index on time scales less than the pulse duration.[37] To evaluate the optical response of silicon metastructure, Keldysh photoionization with a direct bandgap for silicon is considered as the main source for the conduction band carrier density. The refractive index changes are then derived from the Drude-like model with the modified laser-induced electron plasma frequency (see Materials and Methods). First, the homogeneous distribution of free carriers inside silicon nanostructures is assumed. We compare the pump-dependent change of TH wavelength and line width shown in Figure 4a. In the experiment, the TH peak blue-shifts by 0.6 nm with the change of pump power from 20 to 200 GW/cm^2. The measured mode line width increases to two and a half times with a growth of the pump power. Our numerical model (see

https://doi.org/10.1021/acs.nanolett.1c03257
Nano Lett. 2021, 21, 8848−8855

Materials and Methods) predicts a similar change of the line width and peak position shown with solid lines in Figure 4a. We notice that we evaluate the TH line width as a half of the quasi-BIC resonant line width assuming the Lorentz-type resonant dependence of the TH signal. The calculation predicts the increase of the free carrier concentration up to 5×10^{18} cm^{-3} for the pump power density of about 240 GW/cm^2 which corresponds to the power 10 mW. Such high concentration leads to an increase of the plasma frequency which induces the change of refractive index and extinction coefficient shown in Figure 4b. In our initial model, we assume that the distributions of Δn and Δk are uniform within the unit cell. Even with this simplification, the model provides quantitative agreement with the experimental data for the line width and peak blue-shift (Figure 4a). The wavelength change in Figure 4a follows the trend of the refractive index change Δn in Figure 4b, and the same holds for the change of the line width with respect to the change of Δk.

Finally, we extend our theoretical model by implementing 3D simulations based on the FDTD method to couple the propagation effects and carrier generation and account for spatial inhomogeneity of the induced charge density. Similar to our initial simplified model, we consider the multiphoton absorption accounting for Keldysh photoionization[37] with the direct bandgap for silicon as the main source for the conduction band carrier density. The results of 3D FDTD simulations (see Materials and Methods) for the highest pump power density (240 GW/cm^2) are shown in Figure 5. The

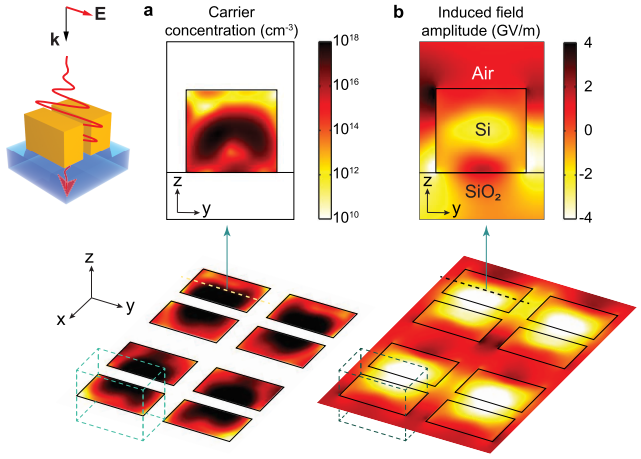

Figure 5. Numerical results. (a) Distribution of the carrier concentration and (b) induced field amplitude within the unit cell of the metasurface for a pump power density of 240 GW/cm^2 at the peak of the pump pulse shown schematically in the upper left corner. The z−y cross sections shown in the upper panels are marked with dashed lines on the x−y plane on the lower panel.

carrier concentration increases to the maximal value of 10^{18} cm^{-3} as shown in Figure 5a at the peak of the pump pulse. The distribution of carriers is nonuniform contrary to our assumptions in calculations for Figure 4a, but as we can see the concentration of carriers is of the same order for both of the calculations. Figure 5b shows the induced field amplitude within the unit cell at the peak of the pump pulse. The characteristic value of the field is of the order of 4×10^9 V/m.

In conclusion, we have observed experimentally, for the first time to our knowledge, the self-action effects of femtosecond laser pulses in the third-harmonic generation from high-Q resonant dielectric metasurfaces. We have shown that the blue-shift of the resonance appears due to multiphoton absorption in silicon resulting in sub- or supercubic dependence of the third-harmonic intensity on the intensity of the incident laser pulse. We have explained the observed phenomena by a strong field ionization in nanostructured silicon that happens on femtosecond time scales. Our results highlight the importance of laser pulse self-action effects for parametric frequency conversion and harmonic generation in dielectric metasurfaces, and they provide useful guidelines for the optimization of designs of nonlinear optical devices.

MATERIALS AND METHODS

Sample Fabrication. The metasurface consists of an array of silicon bar pairs placed on a quartz substrate. First, the SOI wafer (SOITEC) with a top Si layer of 500 nm and a buried SiO_2 layer of 375 nm is cleaned in acetone and isopropybyl alcohol by sonication. A 3 μm SiO_2 layer is deposited on a SOI wafer. The sample is then bonded to a quartz substrate via UV curing of NOA61 as an adhesive layer. The SOI substrate is removed via a deep dry etch and a selective wet etching process. Finally, the bar pairs pattern of the metasurface is defined by e-beam lithography (EBL) technique and then etched by a HBr-based dry etching (PlasmaPro System 100ICP180).

Optical Measurements. The THG measurements are performed with a homemade microscopy setup. For excitation, we use the emission of an optical parametric amplifier (Light Conversion Orpheus-HP) pumped by Yb^{3+} fs laser (Light Conversion Pharos). The central wavelength of 290 fs long laser pulses is scanned in the vicinity of the spectral position of the engineered resonance. THG signal is measured in confocal transmission geometry as shown schematically in Figure 3a. The pump beam with pulse repetition rate of 1 MHz was focused on the sample surface from the substrate side with a 10× Mitutoyo objective, so that 1 mW of average incident power corresponded to 24 GW/cm^2 peak power in the focal spot with diameter of 6 μm. THG emission is collected with a 50× Mitutoyo objective. The IR pump is removed from the collected signal using a short-pass filter (Thorlabs). At higher pump powers, the THG signal is additionally attenuated with a neutral density filter.

Numerical Modeling. Numerical modeling is performed to elucidate the complex transient optical response of the photoexcited metasurface on the basis of 3D nonlinear Maxwell's equations

$$\begin{cases} \dfrac{\partial \vec{E}}{\partial t} = \dfrac{\nabla \times \vec{H}}{\varepsilon_0 \varepsilon} - \dfrac{1}{\varepsilon_0 \varepsilon}(\vec{J}_p + \vec{J}_{Kerr}) \\ \dfrac{\partial \vec{H}}{\partial t} = -\dfrac{\nabla \times \vec{E}}{\mu_0}, \end{cases} \tag{2}$$

where $\vec{E}$ and $\vec{H}$ are the electric/magnetic fields, ε_0 and μ_0 are the free space permittivity and permeability, $\varepsilon = n^2 = 3.45^2$ is the permittivity of the unexcited silicon at 1.5 μm. The Kerr effect is included via the current

$$\vec{J}_{Kerr} = \frac{4}{3}\varepsilon n_2 c \varepsilon_0^2 \frac{\partial(|\vec{E}|^2 \vec{E})}{\partial t} \tag{3}$$

with $n_2 = 4 \times 10^{-18}$ m^2/W at 1.5 μm,[46] and the density current $\vec{J}_p$ includes the optical response of free carriers in the

https://doi.org/10.1021/acs.nanolett.1c03257
Nano Lett. 2021, 21, 8848−8855

conduction band, described by the differential momentum equation

$$\frac{\partial \vec{J}_p}{\partial t} = -\nu_e \vec{J}_p + \frac{e^2 N_e(t)}{m_e^*}\vec{E} \tag{4}$$

where e is the elementary charge, $m_e^* = 0.18m_e$ is the reduced electron−hole mass, and $\nu_e = 1.1 \times 10^{15}$ s^{-1} is the electron collision frequency.[47] For air and fused silica, constant values of refractive indices are used $n_{air}^2 = 1$ and $n_{SiO_2}^2 = 2.08734$ for $\lambda = 1.5$ μm. The system of Maxwell's equations coupled to electron plasma kinetics equations is solved by the finite-difference numerical method,[48] based on FDTD[49] and auxiliary-differential methods for dispersive media.[50] At the edges of the grid, we apply the absorbing boundary conditions related to convolutional perfectly matched layers to avoid nonphysical reflections.[51] The initial electric field is introduced as a Gaussian pulse plane wave

$$E_y(t, x, y) = E_0 \exp\left(-\frac{4\ln 2(t - t_0)^2}{\tau_{FWHM}^2}\right)e^{i\omega t} \tag{5}$$

where $\tau_{FWHM} = 290$ fs, t_0 is the time delay, $\omega = 2\pi c/\lambda$ is the angular frequency, and c is the speed of light. The incident wave propagates along the z-axis, and the laser polarization is directed along the y-axis.

The time-dependent conduction-band carrier density is defined by single-rate equation

$$\frac{\partial N_e}{\partial t} = \frac{N_a - N_e}{N_a} w_{PI} + D_e \Delta N_e - \frac{C_A N_e^3}{C_A \tau_{rec} N_e^2 + 1} \tag{6}$$

where w_{PI} is the Keldysh photoionization rate for silicon with direct bandgap $E_g = 3.4$ eV and $\lambda = 1.5$ μm, $N_a = 5 \times 10^{22}$ cm^{-3} is the silicon atom density, $C_A = 3.8 \times 10^{-31}$ cm^6/s is the Auger recombination rate,[52] $\tau_{rec} = 6 \times 10^{-12}$ s is the minimum Auger recombination time,[53] and $D_e = 18$ cm^2/s is the carrier ambipolar diffusivity.[54]

Numerical simulations are performed on the graphics card Nvidia TITAN RTX with 24 Gb device memory and 4608 CUDA cores. The GPU-based procedure is applied to every spatial point in order to allow simultaneous resolution of the problem (comprising the evolution of the Maxwell equation (2), nonlinear currents (3−4), and carrier density (6)) at each time step ($\approx 1.5 \times 10^5$ temporal steps) on a massive three-dimensional mesh ($\approx 4.2 \times 10^8$ grid points). In order to further optimize the algorithm and reduce the interaction between the neighbor cores during computation, the neighbor spatial values for the fields (required for Maxwell) and carrier densities (for electron diffusion) are prestored at the beginning of each temporal step. This procedure of GPU implementation is detailed in ref 48 and references therein.

AUTHOR INFORMATION

Corresponding Authors

Andrey A. Bogdanov − *School of Physics and Engineering, ITMO University, St. Petersburg 197101, Russia;* orcid.org/0000-0002-8215-0445; Email: bogdan.taurus@gmail.com

Yuri Kivshar − *School of Physics and Engineering, ITMO University, St. Petersburg 197101, Russia; Nonlinear Physics Center, Research School of Physics, Australian National University, Canberra, ACT 2601, Australia;* orcid.org/0000-0002-3410-812X; Email: yuri.kivshar@anu.edu.au

Authors

Ivan S. Sinev − *School of Physics and Engineering, ITMO University, St. Petersburg 197101, Russia;* orcid.org/0000-0002-4246-7747

Kirill Koshelev − *School of Physics and Engineering, ITMO University, St. Petersburg 197101, Russia; Nonlinear Physics Center, Research School of Physics, Australian National University, Canberra, ACT 2601, Australia;* orcid.org/0000-0001-7475-1024

Zhuojun Liu − *State Key Laboratory of Optoelectronic Materials and Technologies, School of Physics, Sun Yat-sen University, Guangzhou 510275, China*

Anton Rudenko − *Arizona Center for Mathematical Sciences and College of Optical Sciences, University of Arizona, Tucson, Arizona 85721, United States*

Konstantin Ladutenko − *School of Physics and Engineering, ITMO University, St. Petersburg 197101, Russia*

Alexey Shcherbakov − *School of Physics and Engineering, ITMO University, St. Petersburg 197101, Russia*

Zarina Sadrieva − *School of Physics and Engineering, ITMO University, St. Petersburg 197101, Russia*

Mikhail Baranov − *School of Physics and Engineering, ITMO University, St. Petersburg 197101, Russia*

Tatiana Itina − *School of Physics and Engineering, ITMO University, St. Petersburg 197101, Russia; Laboratoire Hubert Curien, UMR CNRS 5516/UJM/Université de Lyon, Saint-Etienne 42000, France*

Jin Liu − *State Key Laboratory of Optoelectronic Materials and Technologies, School of Physics, Sun Yat-sen University, Guangzhou 510275, China;* orcid.org/0000-0001-5727-6874

Complete contact information is available at: https://pubs.acs.org/10.1021/acs.nanolett.1c03257

Author Contributions

‡I.S.S. K.K. and Z.L. are equally contributing authors.

Notes

The authors declare no competing financial interest.

ACKNOWLEDGMENTS

Y.K. acknowledges useful comments and suggestions received from Wenshan Cai and Maxim Shcherbakov. Numerical modelling and sample characterization were supported by the Ministry of Science and Higher Education (project 075-15-2021-589). Experimental work was supported by the Russian Science Foundation (project no. 19-72-10086). A.R. acknowledges a support from the Air Force Office of Scientific Research (grant FA9550-19-1-0032). Y.K. acknowledges a support from the Strategic Fund of the Australian National University and the US Army International Office (grant FA5209-21-P0034). K.K. and A.B. acknowledge support from the Foundation for the Advancement of Theoretical Physics and Mathematics "BASIS".

REFERENCES

(1) Kruk, S.; Kivshar, Y. Functional meta-optics and nanophotonics governed by Mie resonances. *ACS Photonics* **2017**, *4*, 2638−2649.

(2) Evlyukhin, A. B.; Reinhardt, C.; Seidel, A.; Luk'yanchuk, B. S.; Chichkov, B. N. Optical response features of Si-nanoparticle arrays. *Phys. Rev. B: Condens. Matter Mater. Phys.* **2010**, *82*, 045404.

(3) Kuznetsov, A. I.; Miroshnichenko, A. E.; Brongersma, M. L.; Kivshar, Y. S.; Luk'yanchuk, B. Optically resonant dielectric nanostructures. *Science* **2016**, *354*, aag2472.
(4) Staude, I.; Schilling, J. Metamaterial-inspired silicon nanophotonics. *Nat. Photonics* **2017**, *11*, 274−284.
(5) Baranov, D. G.; Zuev, D. A.; Lepeshov, S. I.; Kotov, O. V.; Krasnok, A. E.; Evlyukhin, A. B.; Chichkov, B. N. All-dielectric nanophotonics: the quest for better materials and fabrication techniques. *Optica* **2017**, *4*, 814−825.
(6) Koshelev, K.; Kivshar, Y. Dielectric resonant metaphotonics. *ACS Photonics* **2021**, *8*, 102−112.
(7) Wang, S.; Deng, Z.-L.; Wang, Y.; Zhou, Q.; Wang, X.; Cao, Y.; Guan, B.-O.; Xiao, S.; Li, X. Arbitrary polarization conversion dichroism metasurfaces for all-in-one full Poincaré sphere polarizers. *Light: Sci. Appl.* **2021**, *10*, 1−9.
(8) Deng, Z.-L.; Tu, Q.-A.; Wang, Y.; Wang, Z.-Q.; Shi, T.; Feng, Z.; Qiao, X.-C.; Wang, G. P.; Xiao, S.; Li, X. Vectorial Compound Metapixels for Arbitrary Nonorthogonal Polarization Steganography. *Adv. Mater.* **2021**, 2103472.
(9) Qiu, C.-W.; Zhang, T.; Hu, G.; Kivshar, Y. Quo vadis, metasurfaces? *Nano Lett.* **2021**, *21*, 5461−5474.
(10) Maier, S. A. *Plasmonics: Fundamentals and Applications*; Springer Science & Business Media, 2007; pp 1−250.
(11) Schuller, J. A.; Barnard, E. S.; Cai, W.; Jun, Y. C.; White, J. S.; Brongersma, M. L. Plasmonics for extreme light concentration and manipulation. *Nat. Mater.* **2010**, *9*, 193−204.
(12) Koshelev, K.; Lepeshov, S.; Liu, M.; Bogdanov, A.; Kivshar, Y. Asymmetric metasurfaces with high-Q resonances governed by bound states in the continuum. *Phys. Rev. Lett.* **2018**, *121*, 193903.
(13) Campione, S.; Liu, S.; Basilio, L. I.; Warne, L. K.; Langston, W. L.; Luk, T. S.; Wendt, J. R.; Reno, J. L.; Keeler, G. A.; Brener, I.; et al. Broken symmetry dielectric resonators for high quality factor Fano metasurfaces. *ACS Photonics* **2016**, *3*, 2362−2367.
(14) Fedotov, V.; Rose, M.; Prosvirnin, S.; Papasimakis, N.; Zheludev, N. Sharp trapped-mode resonances in planar metamaterials with a broken structural symmetry. *Phys. Rev. Lett.* **2007**, *99*, 147401.
(15) Singh, R.; Al-Naib, I. A.; Yang, Y.; Roy Chowdhury, D.; Cao, W.; Rockstuhl, C.; Ozaki, T.; Morandotti, R.; Zhang, W. Observing metamaterial induced transparency in individual Fano resonators with broken symmetry. *Appl. Phys. Lett.* **2011**, *99*, 201107.
(16) Salary, M. M.; Mosallaei, H. Tunable all-dielectric metasurfaces for phase-only modulation of transmitted light based on quasi-bound states in the continuum. *ACS Photonics* **2020**, *7*, 1813−1829.
(17) Lim, W. X.; Singh, R. Universal behaviour of high-Q Fano resonances in metamaterials: terahertz to near-infrared regime. *Nano Convergence* **2018**, *5*, 1−7.
(18) Forouzmand, A.; Mosallaei, H. All-dielectric C-shaped nanoantennas for light manipulation: Tailoring both magnetic and electric resonances to the desire. *Adv. Opt. Mater.* **2017**, *5*, 1700147.
(19) Yesilkoy, F.; Arvelo, E. R.; Jahani, Y.; Liu, M.; Tittl, A.; Cevher, V.; Kivshar, Y.; Altug, H. Ultrasensitive hyperspectral imaging and biodetection enabled by dielectric metasurfaces. *Nat. Photonics* **2019**, *13*, 390−396.
(20) Jahani, Y.; Arvelo, E.; Yesilkoy, F.; Koshelev, K.; Cianciaruso, C.; De Palma, M.; Kivshar, Y.; Altug, H. Imaging-based spectrometer-less optofluidic biosensor based on dielectric metasurfaces for detecting extracellular vesicles. *Nat. Commun.* **2021**, *12*, 3246.
(21) Bernhardt, N.; Koshelev, K.; White, S. J.; Meng, K. W. C.; Froch, J. E.; Kim, S.; Tran, T. T.; Choi, D.-Y.; Kivshar, Y.; Solntsev, A. S. Quasi-BIC resonant enhancement of second-harmonic generation in WS2 monolayers. *Nano Lett.* **2020**, *20*, 5309−5314.
(22) Lochner, F. J.; George, A.; Koshelev, K.; Bucher, T.; Najafidehaghani, E.; Fedotova, A.; Choi, D.-Y.; Pertsch, T.; Staude, I.; Kivshar, Y.; et al. Hybrid dielectric metasurfaces for enhancing second-harmonic generation in chemical vapor deposition grown MoS_2 monolayers. *ACS Photonics* **2021**, *8*, 218−227.
(23) Cui, C.; Zhou, C.; Yuan, S.; Qiu, X.; Zhu, L.; Wang, Y.; Li, Y.; Song, J.; Huang, Q.; Wang, Y.; et al. Multiple Fano resonances in symmetry-breaking silicon metasurface for manipulating light emission. *ACS Photonics* **2018**, *5*, 4074−4080.
(24) Dixon, J.; Lawrence, M.; Barton, D. R., III; Dionne, J. Self-isolated Raman lasing with a chiral dielectric metasurface. *Phys. Rev. Lett.* **2021**, *126*, 123201.
(25) Mikheeva, E.; Koshelev, K.; Choi, D.-Y.; Kruk, S.; Lumeau, J.; Abdeddaim, R.; Voznyuk, I.; Enoch, S.; Kivshar, Y. Photosensitive chalcogenide metasurfaces supporting bound states in the continuum. *Opt. Express* **2019**, *27*, 33847−33853.
(26) Seok, T. J.; Jamshidi, A.; Kim, M.; Dhuey, S.; Lakhani, A.; Choo, H.; Schuck, P. J.; Cabrini, S.; Schwartzberg, A. M.; Bokor, J.; et al. Radiation engineering of optical antennas for maximum field enhancement. *Nano Lett.* **2011**, *11*, 2606−2610.
(27) Sadrieva, Z. F.; Sinev, I. S.; Koshelev, K. L.; Samusev, A.; Iorsh, I. V.; Takayama, O.; Malureanu, R.; Bogdanov, A. A.; Lavrinenko, A. V. Transition from optical bound states in the continuum to leaky resonances: role of substrate and roughness. *ACS Photonics* **2017**, *4*, 723−727.
(28) Armstrong, J.; Bloembergen, N.; Ducuing, J.; Pershan, P. S. Interactions between light waves in a nonlinear dielectric. *Phys. Rev.* **1962**, *127*, 1918.
(29) Vabishchevich, P. P.; Liu, S.; Sinclair, M. B.; Keeler, G. A.; Peake, G. M.; Brener, I. Enhanced second-harmonic generation using broken symmetry III−V semiconductor fano metasurfaces. *ACS Photonics* **2018**, *5*, 1685−1690.
(30) Koshelev, K.; Tang, Y.; Li, K.; Choi, D.-Y.; Li, G.; Kivshar, Y. Nonlinear metasurfaces governed by bound states in the continuum. *ACS Photonics* **2019**, *6*, 1639−1644.
(31) Liu, Z.; Xu, Y.; Lin, Y.; Xiang, J.; Feng, T.; Cao, Q.; Li, J.; Lan, S.; Liu, J. High-Q quasibound states in the continuum for nonlinear metasurfaces. *Phys. Rev. Lett.* **2019**, *123*, 253901.
(32) Gandolfi, M.; Tognazzi, A.; Rocco, D.; De Angelis, C.; Carletti, L. Near-unity third-harmonic circular dichroism driven by a quasibound state in the continuum in asymmetric silicon metasurfaces. *Phys. Rev. A: At., Mol., Opt. Phys.* **2021**, *104*, 023524.
(33) Zograf, G.; Koshelev, K.; Zalogina, A.; Korolev, V.; Choi, D.-Y.; Zurch, M.; Spielmann, C.; Luther-Davies, B.; Kartashov, D.; Makarov, S.; Kruk, S.; Kivshar, Y. High-harmonic generation from metasurfaces empowered by bound states in the continuum. *arXiv.org* **2020**, 2008.11481. https://arxiv.org/abs/2008.11481
(34) Ghimire, S.; Reis, D. A. High-harmonic generation from solids. *Nat. Phys.* **2019**, *15*, 10−16.
(35) Vampa, G.; McDonald, C.; Orlando, G.; Klug, D.; Corkum, P.; Brabec, T. Theoretical analysis of high-harmonic generation in solids. *Phys. Rev. Lett.* **2014**, *113*, 073901.
(36) Taghinejad, M.; Xu, Z.; Lee, K.-T.; Lian, T.; Cai, W. Transient second-order nonlinear media: Breaking the spatial symmetry in the time domain via hot-electron transfer. *Phys. Rev. Lett.* **2020**, *124*, 013901.
(37) Balling, P.; Schou, J. Femtosecond-laser ablation dynamics of dielectrics: basics and applications for thin films. *Rep. Prog. Phys.* **2013**, *76*, 036502.
(38) Makarov, S.; Kudryashov, S.; Mukhin, I.; Mozharov, A.; Milichko, V.; Krasnok, A.; Belov, P. Tuning of magnetic optical response in a dielectric nanoparticle by ultrafast photoexcitation of dense electron-hole plasma. *Nano Lett.* **2015**, *15*, 6187−6192.
(39) Yang, Y.; Lu, J.; Manjavacas, A.; Luk, T. S.; Liu, H.; Kelley, K.; Maria, J.-P.; Runnerstrom, E. L.; Sinclair, M. B.; Ghimire, S.; Brener, I. High-harmonic generation from an epsilon-near-zero material. *Nat. Phys.* **2019**, *15*, 1022−1026.
(40) Shcherbakov, M. R.; Werner, K.; Fan, Z.; Talisa, N.; Chowdhury, E.; Shvets, G. Photon acceleration and tunable broadband harmonics generation in nonlinear time-dependent metasurfaces. *Nat. Commun.* **2019**, *10*, 1345.
(41) Akhmanov, S. A.; Sukhorukov, A. P.; Khokhlov, R. Self-focusing and diffraction of light in a nonlinear medium. *Soviet Physics Uspekhi* **1968**, *10*, 609.

https://doi.org/10.1021/acs.nanolett.1c03257
Nano Lett. 2021, 21, 8848−8855

(42) Karl, N.; Vabishchevich, P. P.; Shcherbakov, M. R.; Liu, S.; Sinclair, M. B.; Shvets, G.; Brener, I. Frequency conversion in a time-variant dielectric metasurface. *Nano Lett.* **2020**, *20*, 7052−7058.
(43) Zubyuk, V. V.; Shafirin, P. A.; Shcherbakov, M. R.; Shvets, G.; Fedyanin, A. A. Externally driven nonlinear time-variant metasurfaces. *arXiv.org* **2020**, 2012.06604. https://arxiv.org/abs/2012.06604
(44) Melik-Gaykazyan, E.; Koshelev, K.; Choi, J.-H.; Kruk, S. S.; Bogdanov, A.; Park, H.-G.; Kivshar, Y. From Fano to quasi-BIC resonances in individual dielectric nanoantennas. *Nano Lett.* **2021**, *21*, 1765−1771.
(45) Shcherbakov, A. A. GratingFMM. https://github.com/aashcher/GratingFMM (accessed 2021).
(46) Bristow, A. D.; Rotenberg, N.; Van Driel, H. M. Two-photon absorption and Kerr coefficients of silicon for 850−2200 nm. *Appl. Phys. Lett.* **2007**, *90*, 191104.
(47) Sokolowski-Tinten, K.; von der Linde, D. Generation of dense electron-hole plasmas in silicon. *Phys. Rev. B: Condens. Matter Mater. Phys.* **2000**, *61*, 2643.
(48) Rudenko, A.; Colombier, J.-P.; Itina, T. E. Graphics processing unit-based solution of nonlinear Maxwell's equations for inhomogeneous dispersive media. *Int. J. Numer. Modell.: Electronic Networks, Devices and Fields* 2016, e2215.
(49) Yee, K. S. Numerical solution of initial boundary value problems involving Maxwell's equations in isotropic media. *IEEE Trans. Antennas Propag.* **1966**, *14*, 302−307.
(50) Taflove, A.; Hagness, S. C., et al. *Computational electrodynamics: the finite-difference time-domain method*, 2nd ed.; Artech House: MA, 1995; pp 257−270.
(51) Roden, J. A.; Gedney, S. D. Convolution PML (CPML): An efficient FDTD implementation of the CFS-PML for arbitrary media. *Microwave and Optical Technology Letters* **2000**, *27*, 334−339.
(52) Van Driel, H. M. Kinetics of high-density plasmas generated in Si by 1.06-and 0.53-μm picosecond laser pulses. *Phys. Rev. B: Condens. Matter Mater. Phys.* **1987**, *35*, 8166.
(53) Yoffa, E. J. Dynamics of dense laser-induced plasmas. *Phys. Rev. B: Condens. Matter Mater. Phys.* **1980**, *21*, 2415.
(54) Rämer, A.; Osmani, O.; Rethfeld, B. Laser damage in silicon: Energy absorption, relaxation, and transport. *J. Appl. Phys.* **2014**, *116*, 053508.

https://doi.org/10.1021/acs.nanolett.1c03257
Nano Lett. 2021, 21, 8848−8855